Simulation and Validation of Three Dimension Functionally Graded Materials by Material Jetting

Eduardo Salcedo[a]
[a]Department of Mechanical Engineering, Indiana University-Purdue University Indianapolis,799 W. Michigan St., IN, 46202, USA
Email: edsalced@iupui.edu

Dongcheon Baek[b]
[b]Reliability Assessment Center, Korea Institute of Machinery and Materials, 171 Jang-dong, Yuseong-gu
Daejeon, 34103, South Korea
Email: dcbaek@kimm.re.kr

Aaron Berndt[a]
[a]Department of Mechanical Engineering, Indiana University-Purdue University Indianapolis,799 W. Michigan St., IN, 46202, USA
Email: aaberndt@iupui.edu

Jong Eun Ryu[a,c]
[a]Department of Mechanical Engineering, Indiana University-Purdue University Indianapolis,799 W. Michigan St., 46202 IN, USA
[c]Integrated Nanosystems Development Institute, Indiana University-Purdue University Indianapolis, IN, 46202, USA
Email: jeryu@iupui.edu

Corresponding author:

Jong E. Ryu
Department of Mechanical Engineering
Indiana University-Purdue University Indianapolis
723 W Michigan St. Suite SL260
Indianapolis, IN 46202, USA
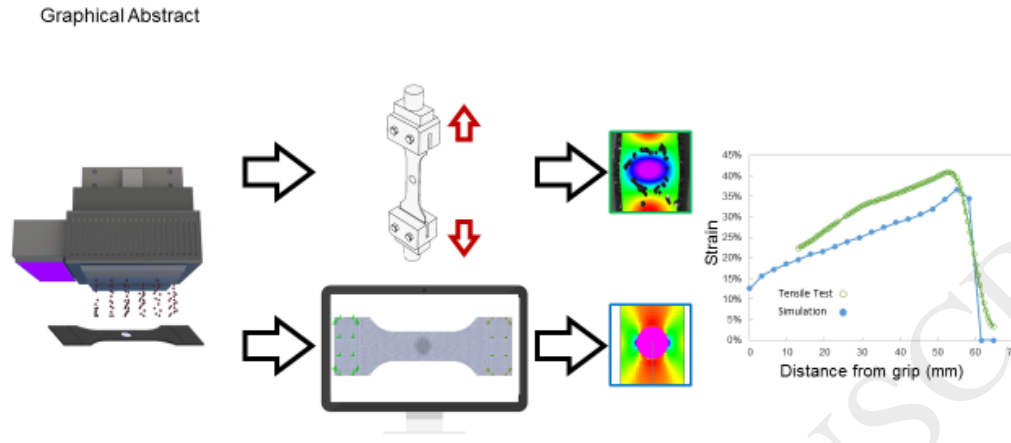e-mail: jeryu@iupui.edu
Tel: 1-317-274-8984

Co-corresponding author:

Dongcheon Baek
Reliability Assessment Center
Korea Institute of Machinery and Materials
171 Jang-dong, Yuseong-gu
Daejeon, 34103, South Korea
Email: dcbaek@kimm.re.kr

_____

Graphical abstract

Graphical Abstract

Highlights

- Modeling of mechanical behavior for the material-jet printed polymers

- Validation of the material models by comparing the finite element analysis and physical tensile test with multi-material printed specimens

- The result proves that it is possible to create a desired strain field by locally changing the ratio of the digital materials without changing the overall shape

Abstract

The goal of this work is to validate the material models for parts created with a Material Jetting 3-dimensional printer through the comparison of Finite Element Analysis (FEA) simulations and physical tests. The strain maps generated by a video extensometer for multi-material samples are compared to the FEA results based on our material models. Two base materials (ABS-like and rubber-like) and their composites are co-printed in the graded tensile test samples. The graded islands are embedded in the rubber-like test specimens. The simulations were conducted

utilizing previously fitted material models, a two-parameter Mooney-Rivlin model for the elastic materials (Tango Black+, DM95, and DM60) and a bilinear model for the rigid material (Vero White+). The results show that the simulation results based on our material models can predict the deformation behaviors of the multi-material samples during a uniaxial tensile test. Our simulation results are able to predict the maximum strain in the matrix material (TB+) within 5% error. Both global deformation pattern and local strain level confirm the validity of the simulated material models.

Keywords

Material jetting, Functionally graded materials, 3-dimensional printing, Additive manufacturing, Finite element analysis, Digital materials

1 Introduction

Additive manufacturing (AM) is a process that creates parts by continuously adding material layer by layer. This technique has been utilized to create complex structures, such as internal hierarchal patterns [1, 2], which are impossible to create with other conventional manufacturing methods. AM has been used in several fields such as dental [3, 4], medical [5-9], aerospace [10, 11], electronics [12], and microfluidics [13, 14] to produce unique devices. As this technology matures, the number of printable materials has greatly increased, making it possible to print reinforced composites [15-17], conductive materials [12], and surgically implantable materials [5, 18].

Material Jetting (MJT) is an AM technique that utilizes piezoelectric nozzles to selectively deposit polymer droplets, which are then cured with UV light [19, 20]. By using multiple material-jetting nozzles, it is possible to create composite materials. Various compositions can be achieved by mixing different ratios of resins prior to the curing phase. These new composite materials, also known as Digital Materials (DM), greatly expand the range of printable materials for the MJT printer. In MJT, the most widely used base materials are Tango Black+ (TB+) and Vero White+ (VW+). TB+ is a rubber-like material capable of large elongation, while VW+ is a rigid material that simulates the mechanical properties of Acrylonitrile Butadiene Styrene (ABS). There are six possible DM combinations printable from the mixture of these two base materials: DM40, DM50, DM60, DM70, DM85, and

DM95. The naming convention is based on the equivalent Shore A hardness of each material. For example, DM60 stands for a Digital Material with Shore A hardness of 60.

MJT is capable of locally tuning material properties to generate Functionally Graded Materials (FGM) [21]. Similar graded materials are naturally observed in the internal structures of bone, the exoskeletons of arthropods, and the bark of trees [22]. These natural graded materials have locally tailored properties that improve their overall performance. Artificially engineered FGMs have mainly focused on the usage of foam materials or metal alloys for the creation of lightweight components [23, 24]. These FGMs have been applied to create aerospace structural materials, lightweight concrete structures, and bone mimicking implants [25, 26]. Modeling of FGMs has been conducted with various different simulation methods, such as percolation theory, fractal analysis, neural networks, swarm optimization, and fuzzy logic [27, 28].

Researchers have recently started to leverage the potential of MJT printing for advanced FGM applications, including robotic mechanisms [29], specialized prosthesis [8, 9], custom tooling [30], mechanical metamaterial [31-33], and multi-material compliant mechanisms [34]. However, the capability of conducting meaningful computer simulations for MJT printed FGMs is limited mainly due to the lack of information regarding the material properties and appropriate material models. MJT manufacturers provide insufficient information on the mechanical properties to conduct FEA simulations.

Most of the past research focused on the effects of the printing parameters on the final mechanical properties of the printed parts. Blanco *et al*. measured the stress relaxation modulus of RGD240 (Stratasys) with respect to the printing angle and orientation [35]. While Adamczak and Bochnia conducted physical testing to validate the stress relaxation models for TB+, VW+ and DM50 [36]. In addition, researchers have studied the effects of aging and print orientation on the mechanical properties of TB+, VW+ and some DMs [37], as well as the fatigue behavior of multi-materials samples [38]. Apart from mechanical properties other characteristics of MJT polymers have been studied such as the thermal conductivities of the base polymers VW+, TB+, and Grey60, the results were subsequently validated through thermal FEA [39]. Dielectric properties for MJT polymers have also been studied by other research laboratories [40]. However, to the best of authors' knowledge, little study has been reported on the material modeling for simulation of DMs created by MJT technology and its subsequent validation through physical testing.

The goal of this study is to validate the developed material models for VW+, TB+, and DMs. This is done through the comparison of simulations and physical tensile test results. In the tensile test samples, various graded structures

were embedded in the elastic TB+ matrix. By comparing the strain maps generated from the FEA simulations and the tensile tests, the deformations in the multi-material samples were analyzed, and the material models were validated. Additionally, the microstructures of the fracture surfaces were analyzed with a scanning electron microscope (SEM) in order to study the interface region between materials.

2 Materials and Methods

The samples were printed utilizing an MJT printer, Connex 500 (Stratasys). Samples were printed utilizing the DM printing mode, which prints at a 30-µm layer height. Both the standard support setting and the matte surface finish option were selected. The matte surface was utilized for better spray painting results, which was required for the video extensometer analysis. The parts were printed lying flat on the build tray with their tensile axis oriented along the printing axis (x-axis). The test samples are composed of TB+, VW+, and two of their DMs (DM95 and DM60, whose Shore A hardness are 95 and 60, respectively). For comparison, a door seal has a Shore A hardness of 55, a tire tread has a value of 70, and a roller skate wheel is around 98.

Material models for these DMs and base materials (TB+, VW+) were developed for FEA simulations in our preliminary study. This characterization process was conducted by fitting tensile test data into a Mooney-Rivlin 2 parameter material model. The uniaxial tensile test was based on the Korean Standard M6518 for vulcanized rubber, which is equivalent to the ASTM D638 test standard. The fitting procedure was done utilizing the fitting capabilities of the Origin Pro software suite.

3-dimensional modeling and FEA simulations were conducted with SolidWorks 2016 (Dassault Systemes). Tensile tests were performed with a 100-series modular universal test machine (UTM, Test Resources). The strain distributions in the samples were analyzed utilizing a video extensometer (Vic Gauge, Correlated Solutions) and its corresponding image analysis software (Vic 2D, Correlated Solutions). The results were then compared to those of the FEA simulations. The microstructures of the samples were analyzed with a SEM (JEOL-7800F).

2.1 Sample design

Fig. 1 shows the dimensions of tensile test specimens. The baseline design, Sample 1 (S1) was printed utilizing only the elastic material (TB+). To discern the effects of multi-material prints, three different configurations were tested. Sample 2 (S2) shown in Fig. 1b consists of the same outline as S1 with the addition of a circular island made up of the rigid material (VW+). In Sample 3 (S3) and Sample 4 (S4) (Figs. 1c-d), graded islands were printed by creating regions of different materials at the center of the samples (VW+, DM95, and DM 60 from the center out). The

circular and rectangular graded islands are embedded within the TB+ in S3 and S4, respectively. The four sample design plans are summarized in Table 1.

(Fig. 1)

(Table 1)

2.2 Tensile Testing

The tensile tests of the printed samples were conducted with a UTM. The displacement was recorded with a video extensometer that measures the distance between markings on sample surface during deformation. The markings were generated by covering the samples with black paint and then by spraying with white spray paint to create a speckled pattern (Fig. 2a). The grips separated at a constant speed of 50 mm/min until the load cell recorded a sudden drop associated with the breakage of the sample or the grip reached the prescribed 30 mm displacement. The video extensometer continuously captured images of the sample as it deformed. These images were then imported into the analysis software. The analysis window (red shaded rectangle in Fig. 2b) was set in the analysis software and allowed for the strain mapping of the sample. The analysis window grows as the sample is stretched as illustrated in Fig. 2c.

 (Fig. 2)

2.3 FEA modeling

Stress-strain curves for TB+, DM95, and DM60 from the uniaxial tensile tests conducted in our preliminary research were fitted into the Mooney-Rivlin two-parameter material model. The Mooney-Rivlin two-parameter model is one of the most widely used phenomenological models for modeling hyper-elastic materials. The fitting equation was:

Eq. 1
$$y = 2 \times \left(1 + \frac{x}{100} - \frac{1}{\left(1+\frac{x}{100}\right)^2}\right) \times \left(C_1 + \frac{C_2}{1+\frac{x}{100}}\right)$$

Where y and x are stress and strain, respectively. C_1 and C_2 represent the elastic behavior and the divert from elasticity, respectively [41]. C_1 and C_2 for the materials used in this study are summarized in Table 2. Fig. 3 shows a comparison between the stress-strain curves from the tensile test data used for the fitting procedure and the material models. TB+ (Fig. 3a) and DM60 (Fig. 3b) have an accurate fit, with DM95 (Fig. 3c) underestimating the stress values at strains lower than 20%. VW+ was modeled as a bilinear material with an initial Young's modulus of 2.0 GPa and yield point of 10 MPa, and a second modulus of 650 MPa and yield point of 30MPa (Fig. 3d).

(Table 2)

(Fig. 3)

SEM images of the fracture surface for VW+ and TB+ show a clear difference between the two materials. The images were taken at 60x (Fig. 4) and 200x (Fig. 5) magnification. TB+ displays a smooth fracture surface with horizontal stripping caused by the layer-by-layer printing. Conversely, the brittle sample of VW+ shows a very rough surface morphology. Both DMs show mostly smooth, but mildly rough surfaces. DM95 displays a rougher fracture surface than DM60 due to the increased amount of VW+ present in the material mixture.

(Fig. 4)

(Fig. 5)

Individual models for each material were imported into the material library of the FEA simulation software and assigned to the corresponding regions shown in Fig. 1. Non-linear studies were used in the FEA to simulate large deformations. The simulation settings are summarized in Table 3. For the boundary conditions, one side of the sample was fixed while the other side was displaced up to 30 mm, mimicking the actual physical test conditions (Fig. 2c). The interface regions between different materials were modeled as perfectly bonded. Due to the mismatch in material properties, the transition regions were modeled with a finer mesh. Fig. 6 shows the center regions of S2 – S4, where the multi-material islands were printed. Details on the mesh parameters and size are summarized in Table 4.

(Table 3)

(Fig. 6)

(Table 4)

3 Results and Discussion

Fig. 7 shows the strain patterns of S1-S4 produced by the extensometer software at 30 mm displacement. At larger deformations, breakage of the paint on the sample surface affects the data acquisition and causes holes on the strain maps. As S1 deformed, it experienced uniform strain levels (Fig. 7a), shown by an almost uniform color throughout the gauge length. In contrast, multi-material samples (S2-S4) exhibited distinct strain patterns caused by the shape of embedded material islands. S2 (Fig. 7b) and S3 (Fig. 7c) display similar strain distributions as they share the same island shape. However, S3, which has a graded transition, displays lower strain values surrounding the VW+ region. The strain gradient shown in S3 is also observed in S4. The different levels of compliance in the DMs surrounding the rigid center cause the gradual transition in both S3 and S4.

(Fig. 7)

The strain patterns produced by the FEA simulation are shown in Fig. 8. The resulting strain patterns for each sample were analogous to those from the tensile test (Fig. 7). The single material sample (S1) showed uniform strain levels throughout the gauge length of the sample. While the multi-material samples displayed unique strain distributions depending on the shape of the embedded island.

S1 displays a maximum strain level of 26%, shown in green throughout its gauge length (Fig. 8a). S2 experiences lower strain levels on the TB+ regions and higher strain levels at VW+ interface (Fig. 8b). S3 shows lower levels of strain immediately surrounding the VW+ region. Each material region experiences varying degrees of strain; with VW+ showing less than 1% strain, DM95 is slightly more compliant and experienced less than 2%. DM60 had a maximum of 20% strain, and TB+ the most elastic material experiences strain in the range of 20% to 40%. S4, which also has a graded transition, displays a similar pattern of strain distributions as S3, with the VW+ region experiencing no strain and each subsequent material region experiencing higher levels of strain.

(Fig. 8)

A comparison of the strain values and locations between the simulation and the physical test for S2-S4 are shown in Fig. 9. The maximum strain in each sample occurred closer to the embedded islands in the simulation results compared to the tensile test results. This disagreement is associated with the geometric assumption in FEA model. The simulation model assumes perfect boundary and bonding between different materials (VW+, DMs, and TB+). However, prior to UV cross-linking phases, the inks diffuse into each other at the interface between the heterogeneous materials. This inter-inks diffusion creates an intermediate region that reduces the abrupt change in material properties at the interface of the embedded island. Both SEM micrographs and visual images confirm the diffusion region between TB+ and VW+ (Fig. 10). The SEM of fracture surface (Fig. 10a) shows an intermediate roughness that is similar with the DMs in Figs. 5b and 5c. The visual image (Fig. 10b) also shows the grey color at the junction area between Tango Black and Vero White due to the diffusion.

The insets of Fig. 9 show the location of rupture after the samples were stretched until the break. Of note, the FEA and tensile test results shown in Figs. 9a-9c were at the fixed displacement of 30 mm. The samples without the graded DM materials (Fig. 9a) broke near the island, while the samples with graded islands (Figs. 9b and 9c) broke away from the TB+ region. This is due to the stress concentration at the non-graded junction reaching the critical rupture stress before other TB regions in the sample. On the other hand, the graded islands reduce the stress around

the islands preventing the rupture of the sample until the background matrix material (TB+) breaks. The TB+ used

in this study breaks at 170% – 220% according to the material data sheet provided by the manufacturer (Stratasys).

(Fig. 9)

(Fig. 10)

A strain level comparison between the simulation results and the tensile test data for S1-S4 is shown in Figs. 11a-d.

The probe points were selected from the center of the sample towards the edge of the analysis window (in the tensile

test) or the grip boundary (in the simulation). From the simulation results 21 probe points were selected at 3.25 mm

intervals, from the tensile test a line was plotted from the center of the sample to the edge of the viewing window

and multiple points along that line were analyzed. As shown in Fig. 11, both physical test and FEA results show

almost identical strain curves.

S1 exhibits a slow decrease in strain as the points move away from the center to the grip (Fig. 11a). S2 displays low

levels of strain at the center of the sample, then as the probe points transition from the VW+ (i region) to the TB+ (iv

region) the strain rapidly increases, approximately to 35% and then slowly decreases (Fig. 11b). Meanwhile the

samples with the gradient transition (S3 and S4) exhibit a gradual change in strain levels as shown in Figs. 11c-f. As

mentioned before, due to model assumptions at material junctions the simulation results have a slight shift in their

respective plots (Figs. 11b-d). The maximum strain is observed at a closer distance from the center in the simulation

results. Additionally, the un-graded island (S2) shows a sharper increase in strain when compared to the graded

island designs (S3 and S4) in both simulation (Fig. 12a) and physical test (Fig. 12b).

(Fig. 11)

(Fig. 12)

With 50% of strain (30-mm displacement in 60-mm gauge length), the maximum strain levels in the materials

(VW+, DM95, DM60, and TB+) the stress distribution was also obtained in the FEA simulation (Figs. 13a-d). While

S1 shows minimal stress concentration throughout the sample (less than 0.2 MPa), the multi-material samples show

concentrations of stress at every material junction.

(Fig. 13)

Conclusion

This research has shown that the FEA method can be utilized to predict the deformation and stress concentrations of

multi-material parts, such as FGMs, printed by the MJT printer. The uniaxial tension test results matched well with

the strain distributions predicted by FEA simulations based on our material models. The material models and FEA methods studied herein facilitate the design of FGMs in advanced applications with high fidelity of predictive analysis. Based on the result of this study, it is possible to create a desired strain field by locally changing the ratio of the DMs without changing the overall shape.

The ability to selectively tune the material properties of a part from rigid to elastic allows for innovative applications. An example is the ability to create living hinges by creating a rigid-elastic-rigid material transition; the stiffness of the hinge can be tailored by using different DMs. It is recommended that intermediate DM materials be added to reduce the stress concentration at the heterogeneous materials junction. Tensile tests conducted until sample break (Fig. 9 insets) show that the multi-material junctions safely withstood large elongations, with the eventual break occurring in the TB+ region at an extreme elongation (>170 %).

Future research will focus on characterizing the material properties when subjected to other load cases, such as compression and shear, to create a cohesive material model. Furthermore, other properties such as dielectric characteristics and conductivity are of special interest in the field of electronics, and therefore must be characterized. As well, special importance will be given to the characterization of the interface regions between different materials. A Nano-indentation experiment at the interface regions to measure the effect of material diffusion on the mechanical characteristics of the boundary is also proposed in the future research.

Acknowledgments

References

1. B.P. Conner, G.P. Manogharan, A.N. Martof, L.M. Rodomsky, C.M. Rodomsky, D.C. Jordan, and J.W. Limperos, Making sense of 3-D printing: Creating a map of additive manufacturing products and services, Additive Manufacturing, 1–4 (2014) 64-76. DOI: https://doi.org/10.1016/j.addma.2014.08.005

2. J. Wu, N. Aage, R. Westermann, and O. Sigmund, Infill Optimization for Additive Manufacturing -- Approaching Bone-like Porous Structures, IEEE Trans Vis Comput Graph, (2017). DOI: 10.1109/TVCG.2017.2655523

3. W.J. van der Meer, A. Vissink, Y.L. Ng, and K. Gulabivala, 3D Computer aided treatment planning in endodontics, J Dent, 45 (2016) 67-72. DOI: 10.1016/j.jdent.2015.11.007

4. D. Anssari Moin, W. Derksen, J.P. Verweij, R. van Merkesteyn, and D. Wismeijer, A Novel Approach for Computer-Assisted Template-Guided Autotransplantation of Teeth With Custom 3D Designed/Printed Surgical Tooling. An Ex Vivo Proof of Concept, J Oral Maxillofac Surg, 74 (2016) 895-902. DOI: 10.1016/j.joms.2016.01.033

5. C.L. Ventola, Medical Applications for 3D Printing: Current and Projected Uses, P T, 39 (2014) 704-711.

6. L.E. Murr, S.M. Gaytan, F. Medina, H. Lopez, E. Martinez, B.I. Machado, D.H. Hernandez, L. Martinez, M.I. Lopez, R.B. Wicker, and J. Bracke, Next-generation biomedical implants using additive manufacturing of complex, cellular and functional mesh arrays, Philos Trans A Math Phys Eng Sci, 368 (2010) 1999-2032. DOI: 10.1098/rsta.2010.0010

7. J. Zuniga, D. Katsavelis, J. Peck, J. Stollberg, M. Petrykowski, A. Carson, and C. Fernandez, Cyborg beast: a low-cost 3d-printed prosthetic hand for children with upper-limb differences, BMC Res Notes, 8 (2015) 10. DOI: 10.1186/s13104-015-0971-9

8. E.L. Doubrovski, E.Y. Tsai, D. Dikovsky, J.M.P. Geraedts, H. Herr, and N. Oxman, Voxel-based fabrication through material property mapping: A design method for bitmap printing, Computer-Aided Design, 60 (2015) 3-13. DOI: 10.1016/j.cad.2014.05.010

9.	H.H. David Moinina Sengeh, A Variable-Impedance Prosthetic Socket for a Transtibial Amputee Designed from Magnetic Resonance Imaging Data, Journal of Prosthetics and Orthotics, 25 (2013) 129-137. DOI: 10.1097/JPO.0b013e31829be19c

10.	J.K. Fuller, STEREOLITHOGRAPHIC ROCKET MOTOR MANUFACTURING METHOD, US 8,844,133 B2, USA, 2014.

11.	S.L.N. Ford, Additive Manufacturing Technology: Potential Implications for U.S. Manufacturing Competitiveness, Journal of International Commerce and Economics, (2014). DOI: https://ssrn.com/abstract=2501065

12.	C.D. Yi Yan, Khai D. T. Ngo, Yuhui Mei, and Guo-Quan Lu. Additive Manufacturing of Planar Inductor for Power Electronics Applications. in International Symposium on 3D Power Electronics Integration and Manufacturing. 2016, Raleigh, NC, USA, IEEE. DOI: 10.1109/3DPEIM.2016.7570536

13.	A.K. Au, W. Huynh, L.F. Horowitz, and A. Folch, 3D-Printed Microfluidics, Angew Chem Int Ed Engl, 55 (2016) 3862-81. DOI: 10.1002/anie.201504382

14.	J.O. Hardin, T.J. Ober, A.D. Valentine, and J.A. Lewis, Microfluidic Printheads for Multimaterial 3D Printing of Viscoelastic Inks, Adv Mater, 27 (2015) 3279-84. DOI: 10.1002/adma.201500222

15.	X. Tian, T. Liu, Q. Wang, A. Dilmurat, D. Li, and G. Ziegmann, Recycling and remanufacturing of 3D printed continuous carbon fiber reinforced PLA composites, Journal of Cleaner Production, 142 (2017) 1609-1618. DOI: 10.1016/j.jclepro.2016.11.139

16.	K. Vidimce, A. Kaspar, Y. Wang, and W. Matusik. Foundry: Hierarchical Material Design for Multi-Material Fabrication. in Proceedings of the 29th Annual Symposium on User Interface Software and Technology. 2016, Tokio, Japan, DOI: 10.1145/2984511.2984516

17.	B.G. Compton and J.A. Lewis, 3D-printing of lightweight cellular composites, Adv Mater, 26 (2014) 5930-5. DOI: 10.1002/adma.201401804

18.   S.Y. Chin, Y.C. Poh, A.-C. Kohler, J.T. Compton, L.L. Hsu, K.M. Lau, S. Kim, B.W. Lee, F.Y. Lee, and S.K. Sia, Additive manufacturing of hydrogel-based materials for next-generation implantable medical devices, Science Robotics, 2 (2017) eaah6451.

19.   J.W. Stansbury and M.J. Idacavage, 3D printing with polymers: Challenges among expanding options and opportunities, Dent Mater, 32 (2016) 54-64. DOI: 10.1016/j.dental.2015.09.018

20.   H. Bikas, P. Stavropoulos, and G. Chryssolouris, Additive manufacturing methods and modelling approaches: a critical review, The International Journal of Advanced Manufacturing Technology, 83 (2015) 389-405. DOI: 10.1007/s00170-015-7576-2

21.   T.R. Jackson, H. Liu, N.M. Patrikalakis, E.M. Sachs, and M.J. Cima, Modeling and designing functionally graded material components for fabrication with local composition control, Materials & Design, 20 (1999) 63-75. DOI: https://doi.org/10.1016/S0261-3069(99)00011-4

22.   P. Fratzl, Biomimetic materials research: what can we really learn from nature's structural materials?, J R Soc Interface, 4 (2007) 637-42. DOI: 10.1098/rsif.2007.0218

23.   G. Udupa, S.S. Rao, and K.V. Gangadharan, Functionally Graded Composite Materials: An Overview, Procedia Materials Science, 5 (2014) 1291-1299. DOI: 10.1016/j.mspro.2014.07.442

24.   A. Chakraborty, S. Gopalakrishnan, and J.N. Reddy, A new beam finite element for the analysis of functionally graded materials, International Journal of Mechanical Sciences, 45 (2003) 519-539. DOI: 10.1016/S0020-7403(03)00058-4

25.   A. Oshkour, N. Abu Osman, Y. Yau, F. Tarlochan, and W. Wan Abas, Design of new generation femoral prostheses using functionally graded materials: a finite element analysis, Proceedings of the Institution of Mechanical Engineers, Part H: Journal of Engineering in Medicine, 227 (2013) 3-17. DOI: 10.1177/0954411912459421

26.   F. Watari, A. Yokoyama, M. Omori, T. Hirai, H. Kondo, M. Uo, and T. Kawasaki, Biocompatibility of materials and development to functionally graded implant for bio-medical application, Composites Science and Technology, 64 (2004) 893-908. DOI: https://doi.org/10.1016/j.compscitech.2003.09.005

27. A.J. Markworth, K.S. Ramesh, and W.P. Parks, Modeling Studies Applied to Functionally Graded Materials, Journal of Materials Science, 30 (1995) 2183-2193. DOI: 10.1007/Bf01184560

28. X.Y. Kou, G.T. Parks, and S.T. Tan, Optimal design of functionally graded materials using a procedural model and particle swarm optimization, Computer-Aided Design, 44 (2012) 300-310. DOI: 10.1016/j.cad.2011.10.007

29. R. MacCurdy, J. Lipton, S. Li, and D. Rus. Printable programmable viscoelastic materials for robots. in Intelligent Robots and Systems (IROS), 2016 IEEE/RSJ International Conference on. 2016, IEEE.

30. A. Kampker, K. Kreisköther, and C. Reinders, Material and Parameter Analysis of the PolyJet Process for Mold Making Using Design of Experiments, World Academy of Science, Engineering and Technology, International Journal of Chemical, Molecular, Nuclear, Materials and Metallurgical Engineering, 11 (2017) 219-226.

31. K. Yu, A. Ritchie, Y. Mao, M.L. Dunn, and H.J. Qi, Controlled Sequential Shape Changing Components by 3D Printing of Shape Memory Polymer Multimaterials, Procedia IUTAM, 12 (2015) 193-203. DOI: 10.1016/j.piutam.2014.12.021

32. A. Ion, J. Frohnhofen, L. Wall, R. Kovacs, M. Alistar, J. Lindsay, P. Lopes, H.-T. Chen, and P. Baudisch. Metamaterial mechanisms. in Proceedings of the 29th Annual Symposium on User Interface Software and Technology. 2016, ACM.

33. A. Ion, L. Wall, R. Kovacs, and P. Baudisch. Digital Mechanical Metamaterials. in Proceedings of the 2017 CHI Conference on Human Factors in Computing Systems. 2017, Denver, Colorado, USA, ACM. DOI: 10.1145/3025453.3025624

34. A.T. Gaynor, N.A. Meisel, C.B. Williams, and J.K. Guest, Multiple-Material Topology Optimization of Compliant Mechanisms Created Via PolyJet Three-Dimensional Printing, Journal of Manufacturing Science and Engineering-Transactions of the Asme, 136 (2014). DOI: 10.1115/1.4028439

35.   D. Blanco, P. Fernandez, and A. Noriega, Nonisotropic experimental characterization of the relaxation modulus for PolyJet manufactured parts, Journal of Materials Research, 29 (2014) 1876-1882. DOI: 10.1557/jmr.2014.200

36.   S. Adamczak and J. Bochnia, Estimating the Approximation Uncertainty for Digital Materials Subjected to Stress Relaxation Tests, Metrology and Measurement Systems, 23 (2016). DOI: 10.1515/mms-2016-0048

37.   B. Lane, S. Moylan, E. Whitenton, and L. Ma, Exploring variability of orientation and aging effects in material properties of multi-material jetting parts, Rapid Prototyp J, 22 (2016) 778-787. DOI: 10.1108/RPJ-11-2015-0169

38.   J.P. Moore and C.B. Williams, Fatigue properties of parts printed by PolyJet material jetting, Rapid Prototyping Journal, 21 (2015) 675-685. DOI: 10.1108/rpj-03-2014-0031

39.   E.C. Mikkelson, Characterization and Modeling of the Thermal Properties of Photopolymers for Material Jetting Processes, in Mechanical Engineering. 2014, Virginia Polytechnic Institute and State University: Blacksburg, Virginia.

40.   W.J. Monzel, B.W. Hoff, S.S. Maestas, D.M. French, and S.C. Hayden, Dielectric Breakdown of Additively Manufactured Polymeric Materials, Ieee Transactions on Dielectrics and Electrical Insulation, 22 (2015) 3543-3549. DOI: 10.1109/Tdei.2015.005199

41.   V.V.R. Nomesh Kumar, Hyperelastic Mooney-Rivlin Model: Determination and Physical Interpretation of Material Constants, MIT International Journal of Mechanical Engineering, 6 (2016) 43-46.

Figure captions

Fig. 1 Dimensions of samples designs: (a) S1, (b) S2, (c) S3, and (d) S4 (Unit: mm).

Fig. 2 Test sample preparation: (a) Samples were covered with black paint and speckled with white spray, (b) Selection of the analysis window in the software, and (c) Image representation of the test procedure.

Fig. 3 Stress-strain curves for the characterization test and the Mooney Rivlin material models for (a) TB+, (b) DM60, (c) DM95, and (d) VW+.

Fig. 4 SEM images of the fracture surface at 60x magnification for (a) TB+, (b) DM60, (c) DM95, and (d) VW+.

Fig. 5 SEM images of the fracture surface at 200x magnification for (a) TB+, (b) DM60, (c) DM95, and (d) VW+.

Fig. 6 Finer mesh control at the interface regions for (a) S2, (b) S3, and (d) S4.

Fig. 7 Strain map results from the video extensometer for (a) S1, (b) S2, (c) S3, and (d) S4. Centerline is shown as a black dotted line.

Fig. 8 Strain map results from the FEA simulation for (a) S1, (b) S2, (c) S3, and (d) S4.

Fig. 9 Visual comparison of strain distribution between FEA simulation and physical tensile tests for (a) S2, (b) S3, and (c) S4 at the displacement of 30 mm. Maximum stress tends to occur closer to the island in FEA simulations. (Inset figures: the images of failure locations when the samples were stretched until break)

Fig. 10 Diffusion of inks at the interface. Mixed regions are boxed with a red-dotted line: (a) SEM cross-sectional view at 100x magnification for the interface between TB+ and VW+; and (b) Cross-sectional image of the interface between TB+ and VW+ with no magnification and a 1 mm scale bar.

Fig. 11 Comparison of strain measurements along the centerline between the tensile test and the simulation results for (a) S1, (b) S2, (c) S3, and (d) S4.

Fig. 12 Comparison of the location of maximum strain for the samples with embedded islands for the (a) tensile test and (b) the simulation.

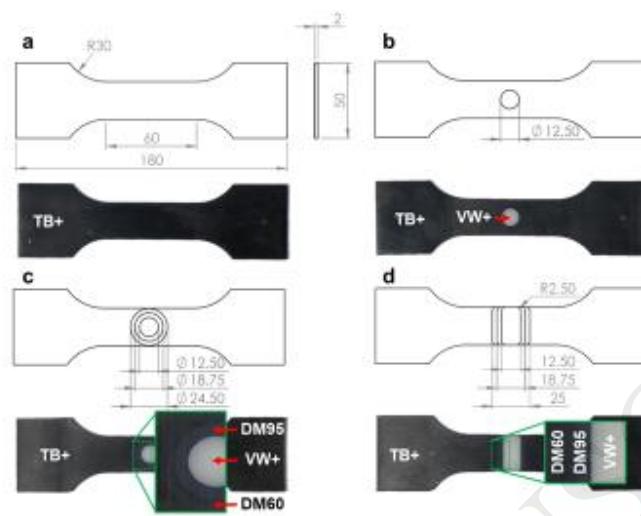Fig. 13 Stress maps from FEA simulation for (a) S1, (b) S2, (c) S3, and (d) S4.
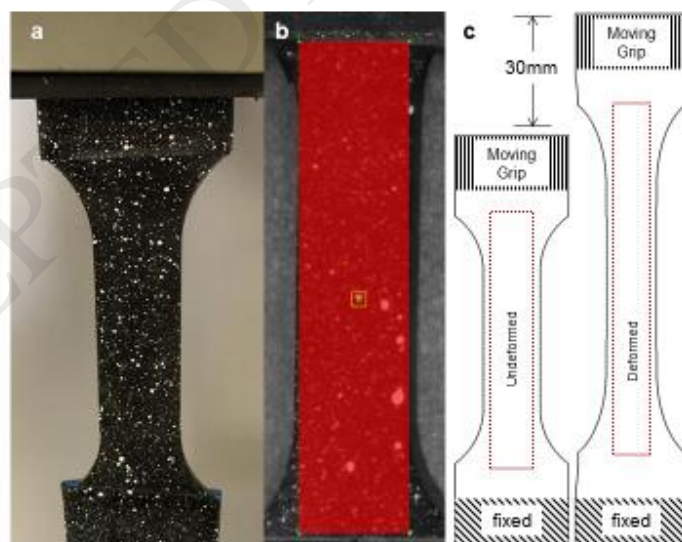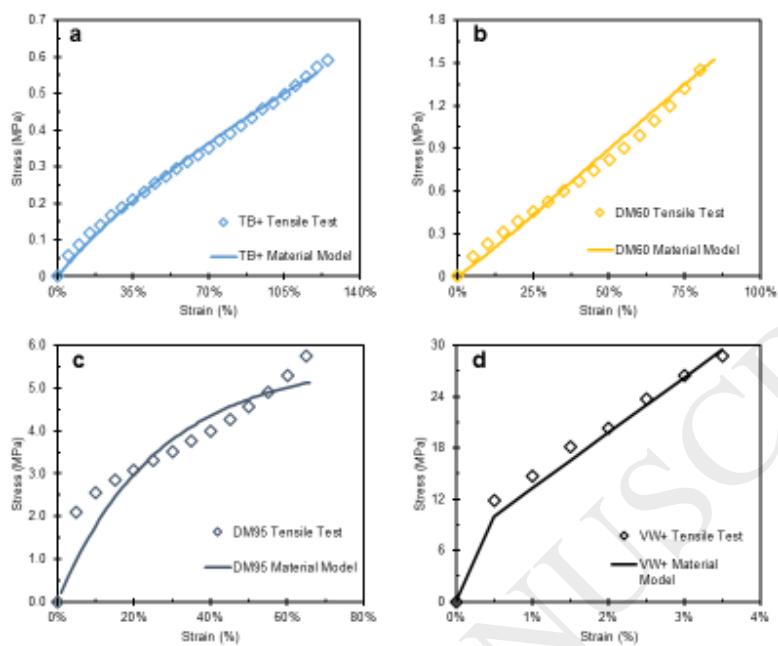
Figure 1
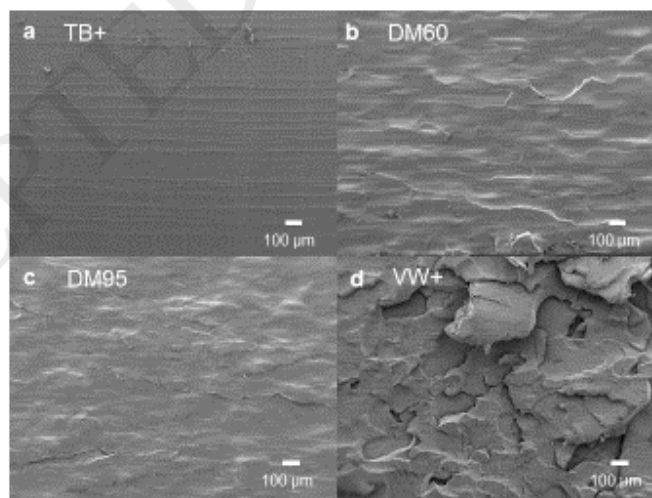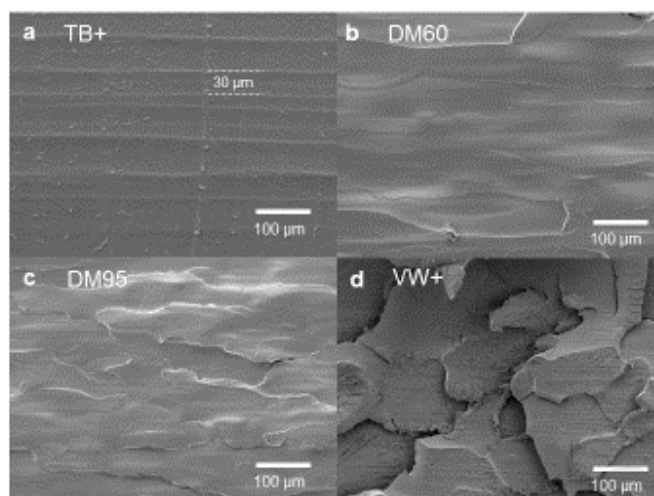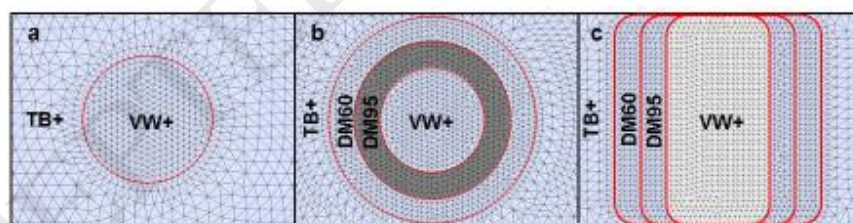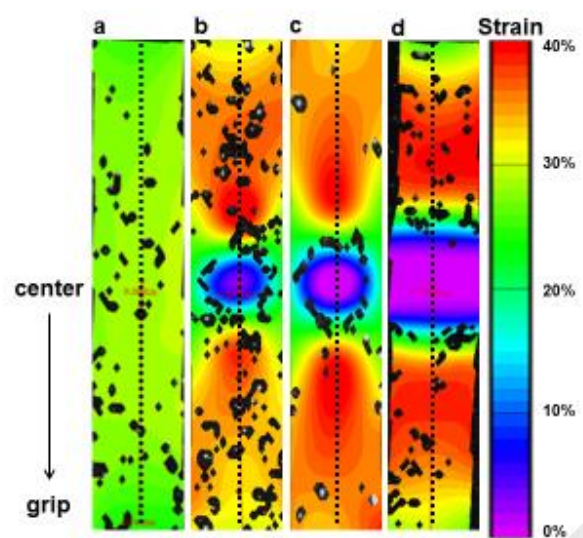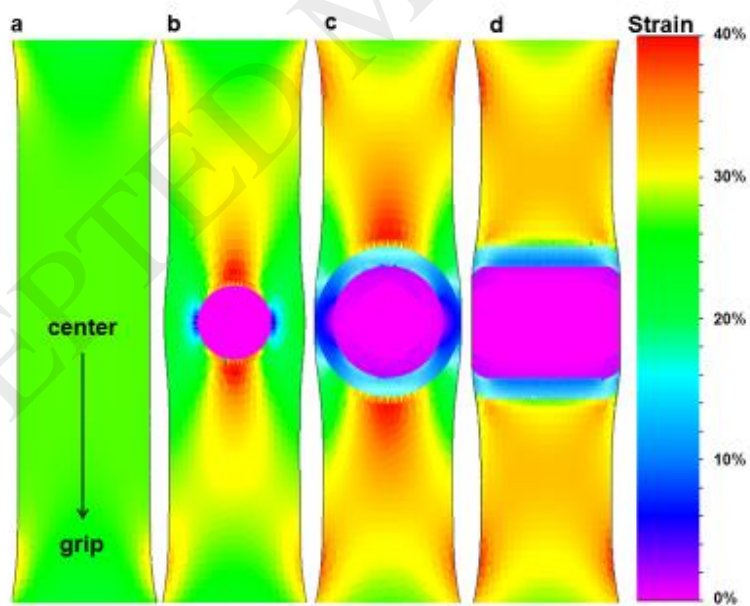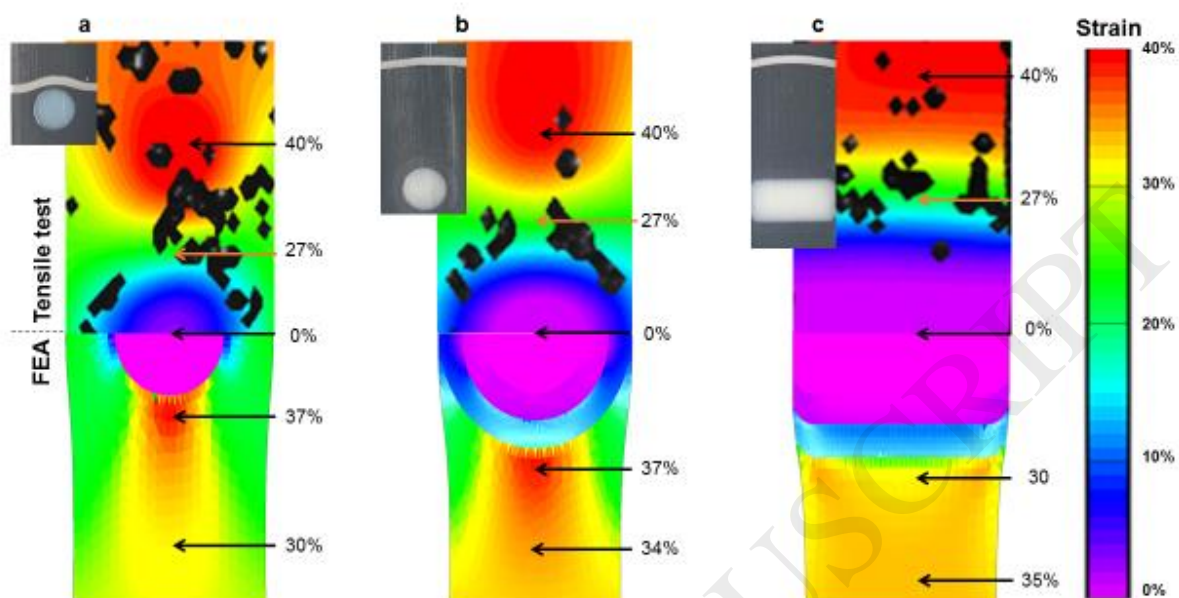

Figure 2
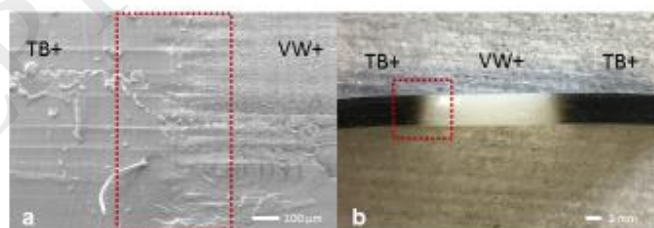
Figure 3

Figure 4

Figure 5

Figure 6

Figure 7

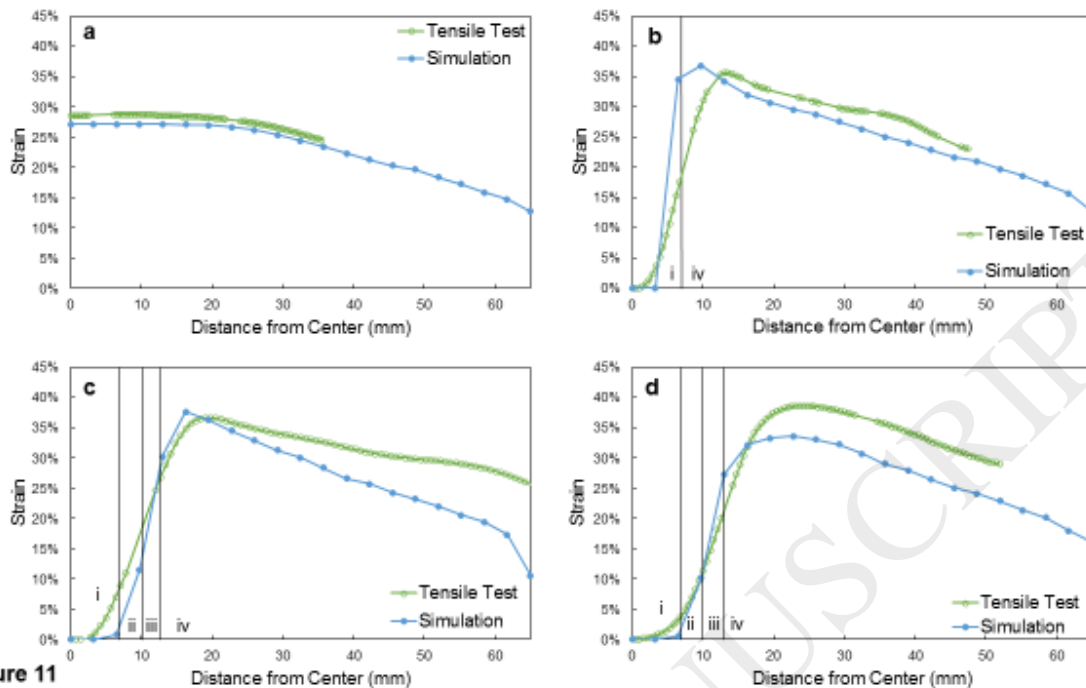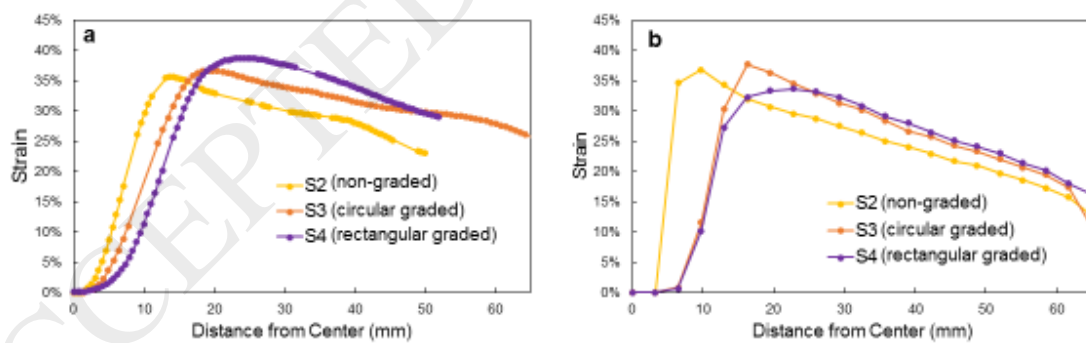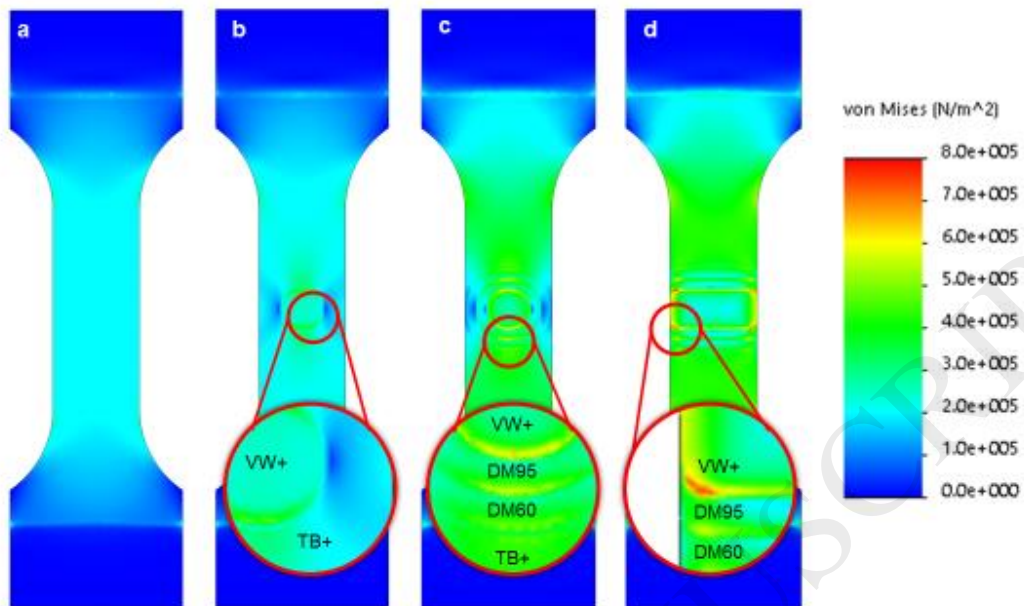Figure 8

Figure 9

Figure 10

Figure 11

Figure 12

Figure 13

List of Tables

Table 1
Description of the shape of the island and gradient type for test samples.

	S1	S2	S3	S4
Island	no	yes	yes	yes
Shape	no	Circle	Circle	Square
Gradient	no	no	yes	yes

Table 2
Material constants for the Mooney-Rivlin model in Eq. 1.

Material	C_1	C_2
TB+	0.15624 MPa	-0.03726 MPa
DM95	-0.54321 MPa	4.18569 MPa
DM60	0.77412 MPa	-0.5262 MPa

Table 3
Finite Element Analysis simulation settings in SolidWorks.

Analysis type	Nonlinear
Mesh type	Solid Mesh
Large displacement formulation	On
Large strain formulation	On
Solver type	FFEPlus
Iterative technique	Newton-Raphson
Integration Method	Newmark

Table 4
Mesh information for the Finite Element Analysis simulation.

Mesh	S1	S2	S3	S4
Mesher	Standard mesh			
Jacobian points	4 Points			
Total Nodes	96113	109159	125763	138239
Total Elements	56658	65476	76786	84362